

# Dynamical parity selection in superconducting weak links

Nico Ackermann,<sup>1</sup> Alex Zazunov,<sup>2</sup> Sunghun Park,<sup>1</sup> Reinhold Egger,<sup>2</sup> and Alfredo Levy Yeyati<sup>1</sup>

<sup>1</sup>*Departamento de Física Teórica de la Materia Condensada, Condensed Matter Physics Center (IFIMAC) and Instituto Nicolás Cabrera, Universidad Autónoma de Madrid, 28049 Madrid, Spain*  
<sup>2</sup>*Institut für Theoretische Physik, Heinrich-Heine-Universität, D-40225 Düsseldorf, Germany*

Excess quasiparticles play a crucial role in superconducting quantum devices ranging from qubits to quantum sensors. In this work we analyze their dynamics for phase-biased finite-length weak links with several Andreev subgap states, where the coupling to a microwave resonator allows for parity state (even/odd) readout. Our theory shows that almost perfect dynamical polarization in a given parity sector is achievable by applying a microwave pulse matching a transition in the opposite parity sector. Our results qualitatively explain key features of recent experiments on hybrid semiconducting nanowire Josephson junctions and provide theoretical guidelines for efficiently controlling the parity state of Andreev qubits.

*Introduction.*—Superconducting Josephson devices are basal ingredients for many of the currently most advanced platforms for quantum information processing and quantum-limited measurements [1–5]. In such devices, non-equilibrium quasiparticles have been identified as one of the main sources of relaxation and decoherence [6], and different techniques have been proposed for mitigating their effect [7–9]. On the other hand, recent fabrication progress on few-channel hybrid nanowires, e.g., semiconducting InAs wires with a superconducting Al shell, has resulted in the wide availability of high-quality tunable superconducting weak links [10–24], harboring Andreev bound states (ABSs) with phase-dependent energy below the pairing gap ( $|\varepsilon| < \Delta$ ) [25–28]. A qubit can be encoded by ABSs [29–33] if the fermion number parity of the Andreev sector (referred to as “parity” below) is conserved. In practice, coherent qubit operation is limited to times shorter than the parity switching time  $\tau_p$  caused, e.g., by transitions between ABSs and above-gap continuum levels. For even-parity [12, 17] as well as odd-parity [18, 19, 21] Andreev qubits, coherent qubit manipulation has already been demonstrated on time scales of order  $\tau_p \sim 100 \mu\text{s}$ . It stands to reason that reaching a thorough understanding of, and thereby good control over, the parity dynamics in superconducting weak links is of fundamental and applied importance.

A remarkable recent experiment [24] has achieved long parity lifetimes together with almost complete dynamical parity polarization. An initial microwave pulse is tuned to induce transitions to an excited many-body Andreev state within the even (or odd) parity sector. After the pulse, deterministic and close-to-ideal parity polarization in the *opposite* odd (even) parity sector has been observed for times  $t \lesssim \tau_p$ , while the steady-state ABS populations are recovered only for  $t \gg \tau_p$  [24]. We here present a unified microscopic theory which qualitatively explains basic experimental observations and can be used as starting point for a more detailed description including, e.g., spin-orbit coupling and electron-electron interaction

effects. We show that for the dynamical parity selection to occur, weak links of intermediate length (harboring at least two ABSs) are needed. While the case of short weak links (with a single ABS) is well understood [34–38], our theory describes the parity dynamics in superconducting weak links of arbitrary length. Focusing on the simplest nontrivial case with two ABSs, we arrive at an intuitive physical picture which identifies wide parameter regimes suitable for dynamical parity selection, and thus for coherent qubit manipulation.

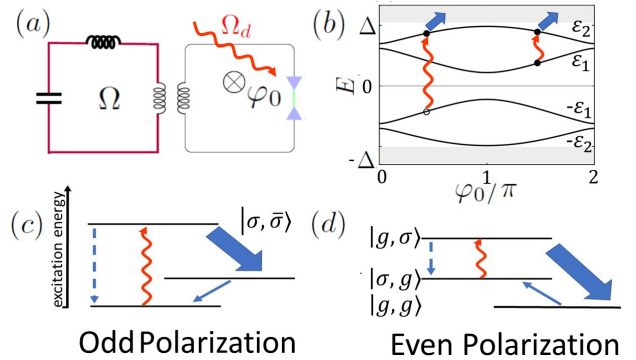


FIG. 1. (a) Schematic setup: a loop containing a finite-length Josephson junction is inductively coupled to a microwave resonator with resonance frequency  $\Omega$ . The flux on the loop imposes the average phase bias  $\varphi_0$  on the junction. In all panels, red wavy lines indicate a microwave pulse with drive frequency  $\Omega_d$ . Solid (dashed) blue arrows show parity-changing (parity-conserving) transitions. The associated rates determine the arrow thickness. (b) ABS energies  $E = \pm\varepsilon_{1,2}$  vs  $\varphi_0$  for junction length parameter  $\ell = 1.3$  and transmission probability  $\mathcal{T} = 0.76$ , see Eq. (13) in the SM [39]. Thick arrows indicate dominant parity-changing transitions due to resonator photon absorption. Panels (c) and (d) show the relevant many-body Andreev states, see Table I, and transition rates for achieving dynamical parity polarization: (c) Excitation of the mixed pair transition  $|g, g\rangle \rightarrow |\sigma, \bar{\sigma}\rangle$  induces odd-parity polarization. (d) Excitation of the odd-parity transition  $|\sigma, g\rangle \rightarrow |g, \sigma\rangle$  leads to even-parity polarization.

$ \alpha, \beta\rangle$	$E_{\alpha, \beta}$	Parity	$ \alpha, \beta\rangle$	$E_{\alpha, \beta}$	Parity
$ g, g\rangle$	0	even	$ \sigma, g\rangle$	$\varepsilon_1$	odd
$ e, g\rangle$	$2\varepsilon_1$		$ g, \sigma\rangle$	$\varepsilon_2$	
$ \sigma, \sigma'\rangle$	$\varepsilon_1 + \varepsilon_2$		$ e, \sigma\rangle$	$2\varepsilon_1 + \varepsilon_2$	
$ g, e\rangle$	$2\varepsilon_2$		$ \sigma, e\rangle$	$\varepsilon_1 + 2\varepsilon_2$	
$ e, e\rangle$	$2\varepsilon_1 + 2\varepsilon_2$				

TABLE I. Many-body Andreev states  $|\alpha, \beta\rangle$  with energy  $E_{\alpha, \beta}$  for a weak link with two ABSs at fixed  $\varphi_0$ , see Fig. 1(b). The first (second) index  $\alpha$  ( $\beta$ )  $\in \{g, e, \sigma = \pm\}$  refers to the occupation of the ABS pair with energy  $\pm\varepsilon_1$  ( $\pm\varepsilon_2$ ).

*Basic picture.*—As schematically shown in Fig. 1(a), we consider a single-channel superconducting weak link embedded in a loop geometry and coupled to an LC circuit. The average phase difference  $\varphi_0$  is related to the magnetic flux threading the loop. The weak link has the length  $L = \ell\xi_0$ , with the coherence length  $\xi_0 = v_F/\Delta$  and the Fermi velocity  $v_F$  (we put  $\hbar = e = k_B = 1$ ). For a short link with  $\ell \ll 1$ , it is well known that a single ABS with particle-hole symmetric energy levels  $\pm\varepsilon(\varphi_0)$  exists [28], where  $0 \leq \varepsilon(\varphi_0) < \Delta$ . In the semiconductor picture [35], there are four many-body Andreev states at fixed  $\varphi_0$ : (i) for the ground state  $|g\rangle$  with  $E_g = 0$ , taken as the reference energy for fixed  $\varphi_0$ , only the  $-\varepsilon$  level is occupied; (ii) for the excited state  $|e\rangle$  with  $E_e = 2\varepsilon$  and the same (even [35]) parity, only the  $+\varepsilon$  level is occupied; (iii) for the odd-parity states  $|\sigma = \pm\rangle$  with  $E_\sigma = \varepsilon$ , the  $\pm\varepsilon$  levels are either both empty or both occupied. On the other hand, for a link of intermediate length  $\ell \sim 1$ , one typically finds *two* ABSs with  $0 \leq \varepsilon_1(\varphi_0) \leq \varepsilon_2(\varphi_0) < \Delta$ , as illustrated in Fig. 1(b). The resulting 16 many-body Andreev states are specified in Table I. Compared to the short-junction limit, longer junctions harboring at least two ABSs allow for qualitatively new phenomena such as dynamical parity polarization. Our theory addresses precisely this situation.

In Fig. 1(c), we show the relevant states for generating odd-parity polarization together with the dominant transition rates due to photon-induced mixing of ABSs and continuum states. Here the initial pulse is assumed resonant with the  $|g, g\rangle \leftrightarrow |\sigma, \bar{\sigma}\rangle$  transition, where  $\sigma' = \bar{\sigma} = -\sigma$  in Table I because of spin conservation. The drive frequency is thus given by  $\Omega_d = \varepsilon_1 + \varepsilon_2$ . If spin-orbit and Coulomb interactions are neglected, such transitions are degenerate with the  $|\sigma, g\rangle \leftrightarrow |e, \sigma\rangle$  transition in the odd sector, which could then be excited simultaneously. However, even mild interactions are known to remove such degeneracies [23]. We further discuss this issue in the SM [39]. If the excited state is connected to the lowest-energy odd-parity state by a parity-changing transition rate  $\Gamma_{|\sigma, \bar{\sigma}\rangle \rightarrow |\sigma, g\rangle}$  exceeding the relaxation rate into the even-parity ground state, the system is quickly driven into the odd-parity sector with almost ideal polarization. The much smaller rate

$\Gamma_{|\sigma, g\rangle \rightarrow |g, g\rangle}$  then only establishes the final steady-state population reached at very long times  $t \gg \tau_p$ . A similar picture applies for the dynamical stabilization of the even-parity sector, see Fig. 1(d). Our formalism allows us to identify optimal parameters for achieving dynamical parity selection. For instance, a key criterion is to have the upper ABS manifold with energy  $\varepsilon_2(\varphi_0)$  within an energy range  $\sim \Omega$  near the continuum threshold  $\varepsilon = \Delta$ , together with temperatures comparable to the resonator frequency  $\Omega$ . Under these conditions, a thermally activated photon is available, photon absorption becomes effective, and parity-changing transitions are favored over parity-conserving ones.

*Model.*—We study a phase-biased superconducting weak link given by a nanowire Josephson junction embedded in a loop geometry and coupled to the electromagnetic phase fluctuations of an LC circuit, see Fig. 1(a). In the standard Andreev approximation [28], the Hamiltonian  $H_{L/R}$  for the  $s$ -wave BCS superconductor on the left ( $x < 0$ ) or right ( $x > 0$ ) side of the contact is expressed by quasiclassical Nambu spinor envelopes  $\psi_\pm(x, t)$  for right- and left-movers with Fermi momentum  $\pm k_F$ , respectively. With  $s_{L/R} = \pm 1$  and Pauli matrices  $\tau_{x,y,z}$  in Nambu space, and assuming the same pairing gap  $\Delta$  on both sides, one finds [28, 32, 35]

$$H_{j=L/R}(t) = \sum_{\pm} \int_{s_j x < 0} dx \psi_\pm^\dagger(x, t) (\mp i v_F \tau_z \partial_x + V_j(t) \tau_z + \Delta \tau_x e^{i\tau_z \phi_j(t)}) \psi_\pm(x, t), \quad (1)$$

where the fluctuating voltages  $V_j(t)$  and phases  $\phi_j(t)$  are linked by the Josephson relation,  $V_j = \dot{\phi}_j/2$ , and the gauge-invariant phase difference across the contact is  $\varphi(t) = \phi_L - \phi_R$ . Modeling the weak link as a normal-conducting constriction with length  $L = \ell\xi_0$  and transmission probability  $\mathcal{T}$  due a local scatterer, the quasiclassical envelopes on both sides of the contact ( $x = 0^\pm$ ) are matched by a transfer matrix [28, 32, 35],

$$\sqrt{\mathcal{T}} \begin{pmatrix} \psi_+(0^-, t) \\ \psi_-(0^-, t) \end{pmatrix} = \begin{pmatrix} e^{-i\tau_z \hat{\theta}_R} & r \\ r & e^{i\tau_z \hat{\theta}_R} \end{pmatrix} \begin{pmatrix} \psi_+(0^+, t) \\ \psi_-(0^+, t) \end{pmatrix} \quad (2)$$

with the reflection amplitude  $r = \sqrt{1 - \mathcal{T}}$  and the dynamical phase shift  $\hat{\theta}_R(t) = \hat{\theta}(t) - \frac{L}{2v_F} \dot{\phi}_R(t) \tau_z$ , where  $\hat{\theta} = \frac{L}{v_F} i \partial_t = \ell\omega/\Delta$ . Equation (7) assumes a symmetric contact with a local scatterer at the center of the weak link. The generalization to arbitrary impurity position is straightforward [39]. Since our conclusions are robust when changing this position, we focus on the symmetric case below.

We next write  $\varphi(t) = \varphi_0 + \tilde{\varphi}(t)$  with  $|\tilde{\varphi}(t)| \ll 1$ , where  $\tilde{\varphi}(t)$  describes electromagnetic phase fluctuations. Choosing the gauge  $\phi_{L/R}(t) = \pm\varphi(t)/2$ , we proceed [39] by expanding  $H_j(t)$  to linear order in  $\tilde{\varphi}$ , gauging away  $\dot{\tilde{\varphi}}$  from the matching condition (7), and expanding to linear

order also in  $\tilde{\varphi}$ . Finally, the phase difference  $\varphi_0$  is gauged away from  $H_j(t)$  such that  $\varphi_0$  appears only through the transfer matrix. For  $\tilde{\varphi} = 0$ , one arrives at the analytically solvable Bogoliubov-de Gennes (BdG) equations

$$\begin{aligned} (-iv_F\tau_z\sigma_z\partial_x + \Delta\tau_x)\Psi_\nu(x) &= \varepsilon_\nu\Psi_\nu(x), \\ \sqrt{\mathcal{T}}\Psi_\nu(0^-) &= e^{i\tau_z\varphi_0/2}(e^{-i\tau_z\sigma_z\theta_\nu} + r\sigma_x)\Psi_\nu(0^+), \end{aligned} \quad (3)$$

where the stationary eigenstates  $\Psi_\nu(x)$  for energy  $\varepsilon_\nu$  are bispinors in Nambu and left-right mover space, Pauli matrices  $\sigma_{x,y,z}$  act in left-right mover space, and  $\theta_\nu = \ell\varepsilon_\nu/\Delta$ . The solution of Eq. (3) defines the noninteracting Hamiltonian  $H_0$ . The quantum numbers  $\nu$  include subgap ABS solutions,  $\nu = \pm m$  with  $m = 1, \dots, N$  and  $\varepsilon_\nu = \pm\varepsilon_m(\varphi_0)$ , see Eq. (13) in the SM [39]. An example with  $N = 2$  ABS pairs is shown in Fig. 1(b). Above-gap continuum quasiparticles are instead labeled by  $\nu = (\varepsilon, s)$  with  $|\varepsilon| > \Delta$  and  $s \in \{1, 2, 3, 4\}$  for an electron or hole incoming from the left or right side.

From the above steps, we find  $H_c = \frac{1}{2}\mathcal{I}\tilde{\varphi}$  for the coupling to phase fluctuations, where the supercurrent operator  $\mathcal{I}$  has the matrix elements

$$\mathcal{I}_{\nu\nu'} = \int dx \operatorname{sgn}(-x)\Psi_\nu^\dagger\left(\frac{\omega_{\nu\nu'}}{2i}(\tau_z - \ell\tau_y\sigma_z) + \Delta\tau_y\right)\Psi_{\nu'} \quad (4)$$

with  $\omega_{\nu\nu'} = \varepsilon_\nu - \varepsilon_{\nu'}$ . The full Hamiltonian,  $H = H_0 + H_c + H_{\text{bath}}$ , also includes an oscillator bath term for the electromagnetic environment [28, 40, 41], for which we assume a thermal equilibrium state at temperature  $T_{\text{env}}$ . For the setup in Fig. 1(a), with resonance frequency  $\Omega$ , dimensionless coupling strength  $\kappa$ , and damping constant  $\eta$ , the bath spectral density is taken as [35, 40]

$$J(\omega) = \frac{\kappa^2\eta}{2\pi} \left( \frac{1}{(\omega - \Omega)^2 + \frac{\eta^2}{4}} - \frac{1}{(\omega + \Omega)^2 + \frac{\eta^2}{4}} \right) + J_{\text{ohm}}. \quad (5)$$

For a realistic comparison with experimental results, we here also include a background Ohmic spectral density,  $J_{\text{ohm}}(\omega) = \alpha_0\omega e^{-|\omega|/\omega_c}$  [40, 41], with dimensionless coupling  $\alpha_0 \ll 1$  and high-frequency cutoff  $\omega_c \approx \Delta$ .

*Master equation.*—We now turn to the dynamics of the density matrix  $\rho(t)$  in the fermion sector, which follows after tracing over the bath. We consider temperatures large against all microscopic transition rates, which for our system parameters implies  $T_{\text{env}} \gtrsim 10^{-2}\Delta$ , and weak system-bath coupling,  $\kappa \ll 1$ . Under these conditions, the Born-Markov approximation applies and a sequence of standard steps [39–41] gives a Lindblad equation for  $\rho(t)$ . In order to arrive at tractable expressions, following the arguments in Ref. [35], we neglect entanglement between Andreev and continuum quasiparticles. Modeling the presence of excess continuum quasiparticles by a quasi-equilibrium Fermi distribution with effective quasiparticle temperature  $T_{\text{qp}}$ , which can differ from (and typically will exceed)  $T_{\text{env}}$ , we can also trace over the continuum quasiparticle sector.

As a consequence, the density matrix describing the Andreev sector,  $\rho_A(t)$ , obeys a simpler Lindblad equation with source terms describing transitions from or into the continuum sector [39].

As final step, we project the dynamical equation for  $\rho_A$  onto the many-body Andreev states  $|\alpha, \beta\rangle$  listed in Table I. The diagonal elements of  $\rho_A$  contain the respective occupation probabilities,  $P_{\alpha,\beta}(t) = \langle\alpha, \beta|\rho_A(t)|\alpha, \beta\rangle$ , which are combined to form a 16-dimensional vector  $\mathbf{P}(t)$ . Since the dynamics of the off-diagonal part of  $\rho_A$  decouples from  $\mathbf{P}(t)$ , we obtain a matrix rate equation,  $\dot{\mathbf{P}} = \mathbf{M}\mathbf{P}$ , with the symmetric  $16 \times 16$  matrix  $\mathbf{M}$  explicitly given in the SM [39], where we also describe simplifications due to state degeneracies in Table I, e.g.,  $P_{+,g} = P_{-,g}$ . Given the eigenvalues  $\lambda_n \leq 0$  and the corresponding eigenvectors  $\mathbf{P}_n$  of  $\mathbf{M}$ , we arrive at the solution  $\mathbf{P}(t) = \sum_n c_n e^{\lambda_n t} \mathbf{P}_n$ , where the initial configuration  $\mathbf{P}(0)$  is determined by the real coefficients  $c_n$ . The total odd-parity probability,  $P_{\text{odd}}(t)$ , follows from this solution by summing over all odd-parity states, with  $P_{\text{even}} = 1 - P_{\text{odd}}$  for the even-parity sector. For the numerical results shown below, we consider a weak link with  $\ell = 1.3$  and  $\mathcal{T} = 0.76$ , where the ABS spectrum is shown in Fig. 1(b). The parameters entering  $J(\omega)$  in Eq. (5) were chosen as

$$\Omega = 0.13\Delta, \quad \kappa = 0.1, \quad \eta = 10^{-4}\Delta, \quad \alpha_0 = 10^{-3}. \quad (6)$$

This parameter choice is aimed at describing, at least qualitatively, the experimental situation in Ref. [24]. However, as discussed below and in the SM [39], our general conclusions are robust against parameter changes.

*Steady-state behavior.*—We first address the steady state reached for  $t \rightarrow \infty$ . In Fig. 2(a), we show results for the probability difference  $\Delta P(\infty) \equiv P_{\text{even}}(\infty) - P_{\text{odd}}(\infty)$  as color-scale plot in the  $T_{\text{env}}-T_{\text{qp}}$  plane for  $\varphi_0 = \pi$ . We observe that the odd-parity sector becomes favorable for large ratio  $T_{\text{qp}}/T_{\text{env}}$ , which can be rationalized by noting that excess continuum quasiparticles can then proliferate. Although much more suppressed, such a population inversion can also occur in short weak links with only a single ABS pair, see the inset of Fig. 2(a). We emphasize that the steady state typically does *not* allow for a large parity polarization in the odd-parity sector. As we illustrate in Fig. 2(b), this only partial steady-state parity polarization in addition strongly depends on the phase difference  $\varphi_0$ .

*Dynamical parity polarization.*—We now consider the system dynamics after preparing an initial state simulating the effect of a resonant driving pulse, see Fig. 1. For simplicity, we here assume that a microwave pulse with drive frequency  $\Omega_d$  matching a transition in a given parity sector causes a complete population inversion in that sector while leaving the other one unaffected, see the SM [39] for a detailed discussion. The initial state  $\mathbf{P}(0)$  immediately after the pulse

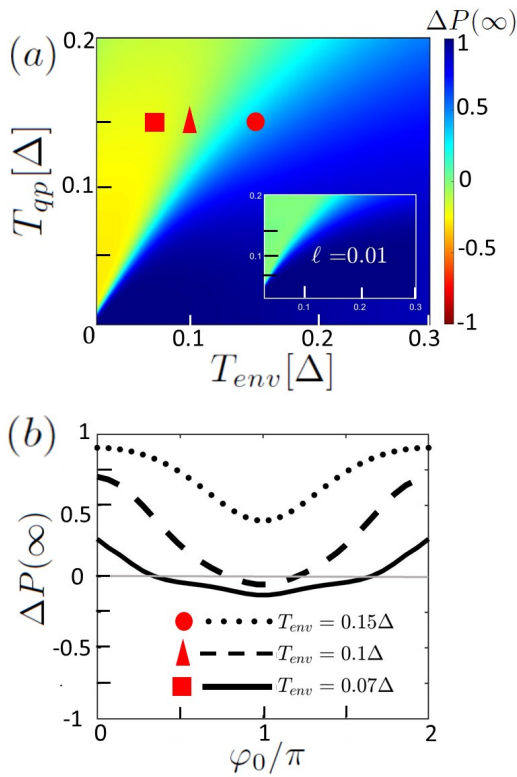


FIG. 2. Difference  $\Delta P(\infty) = P_{\text{even}}(\infty) - P_{\text{odd}}(\infty)$  of the steady-state parity probabilities for  $\ell = 1.3$ ,  $\mathcal{T} = 0.76$ , and the parameters (6). (a) Color-scale plot of  $\Delta P(\infty)$  in the  $T_{\text{env}}-T_{\text{qp}}$  plane for  $\varphi_0 = \pi$ . The inset shows the corresponding results for  $\ell = 0.01$  and otherwise identical parameters. (b)  $\Delta P(\infty)$  vs  $\varphi_0$  for  $T_{\text{qp}} = 0.15\Delta$  and three different values of  $T_{\text{env}}$ .

then preserves the overall steady-state probabilities  $P_{\text{odd,even}}(\infty)$ . In Fig. 3 we illustrate the resulting time evolution after the driving pulse. Panels (a) and (c) correspond to the case where the driving pulse matches the mixed-pair transition in the even parity sector (at fixed  $\varphi_0$ ) and the odd-parity stabilization mechanism in Fig. 1(c) operates: due to the energetic proximity to the continuum, the relaxation from the excited state  $|\sigma, \bar{\sigma}\rangle$  proceeds much faster to the odd-parity ground state  $|\sigma, g\rangle$  than to the even-parity ground state  $|g, g\rangle$ . While the dynamical polarization stabilization is most effective for  $\varphi_0 \sim \pi$ , it remains robust over a broad phase range as shown in panel (c). We note that side features with enhanced parity polarization are seen for  $\Omega \approx \Delta - \varepsilon_2(\varphi_0)$ . For the chosen parameter set, we obtain dynamical odd-parity polarizations  $P_{\text{odd}} \gtrsim 0.98$  on time scales of order  $100\mu\text{s}$ . The Ohmic background in  $J(\omega)$ , although not essential for the main effect, is necessary to obtain time scales as in the experiments of Ref. [24]. Similarly, panels (b) and (d) illustrate the corresponding effect when exciting the odd-parity transition  $|\sigma, g\rangle \rightarrow |g, \sigma\rangle$ . In this case one obtains almost full dynamical polarization

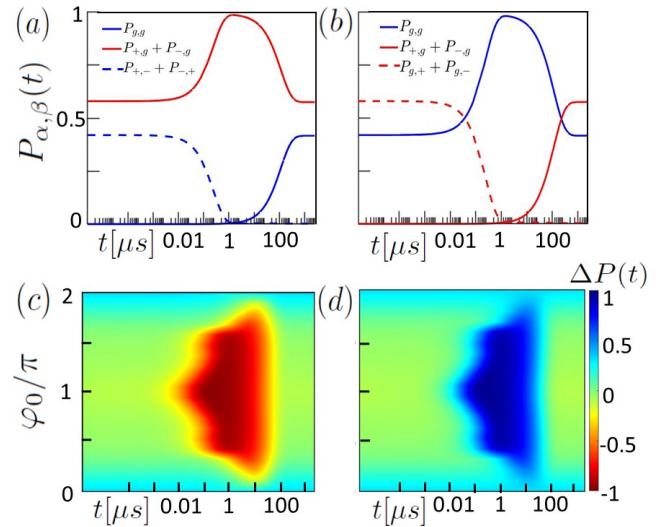


FIG. 3. Dynamical polarization after the initial microwave pulse, see Fig. 1, for the parameters in Fig. 2 with  $T_{\text{qp}} = 0.15\Delta$  and  $T_{\text{env}} = 0.07\Delta$ . (a) Dominant occupation probabilities  $P_{\alpha,\beta}(t)$  vs  $t$  (time in  $\mu\text{s}$ , on logarithmic scale) for  $\varphi_0 = \pi$  and the case shown in Fig. 1(c), resulting in dynamical polarization of the odd-parity sector. Even-parity (odd-parity) states are shown in blue (red) color. Dashed curves indicate excited states in the respective sector. (b) Same but for polarization of the even-parity sector, see Fig. 1(d). (c) Color-scale plot of  $\Delta P(t) = P_{\text{even}}(t) - P_{\text{odd}}(t)$  in the  $t$ - $\varphi_0$  plane for the case in panel (a). (d) Same as in panel (c) but for polarization of the even-parity sector.

in the even-parity sector, which persists on a similar time scale  $\sim 100\mu\text{s}$ . Additional predictions for other parameters are shown in the SM [39] and suggest that our conclusions do not require fine tuning.

We also find that the above dynamical polarization mechanism remains robust over a broad temperature range. However, particularly strong polarization effects are obtained for  $T_{\text{qp}} \gtrsim T_{\text{env}}$ , where only the ground states in each parity sector are populated in the steady state. The couplings  $\kappa$  and  $\alpha_0$  then control the parity lifetimes.

In the SM [39], we show that for a continuous microwave drive with frequency  $\Omega_d$  and amplitude  $g_d$ , our theory gives very similar results for the achievable polarization values as under the idealized initialization approach, with only weak dependence on  $g_d$  for  $10^{-6}\Delta \lesssim g_d \ll \Omega_d$ . These results are in line with the observations in Ref. [24], i.e., optimal polarization requires a certain minimal drive amplitude and decreases with the delay time. We cannot exclude, however, that multi-photon processes (not included in our modeling) are needed for a more quantitative explanation of the results in Ref. [24]. Finally, at elevated temperatures, we find that a polarization in the odd sector can also be generated by driving the excited transition  $|e, g\rangle \rightarrow |\sigma, \bar{\sigma}\rangle$ , with drive frequency  $\Omega_d = \varepsilon_2 - \varepsilon_1$ , which may help to explain experimental observations in Ref. [24].

*Conclusions.*—Our theory suggests a simple physical mechanism for inducing almost perfect dynamical parity polarization of the subgap states in finite-length Josephson junctions. This effect should be useful in facilitating Andreev qubit quantum manipulations within a protected parity subspace. Although we have considered a simplified model which neglects many aspects of realistic devices, the mechanism discussed here provides a basis for qualitatively understanding the intriguing experimental results of Ref. [24]. Our predictions on the phase dependence, see Figs. 3(c,d), as well as on the dependence on temperature  $T_{\text{env}}$  and resonator frequency  $\Omega$ , see the SM [39], could be tested by future experiments, where the proposed mechanism also offers a simple strategy for optimizing the parity polarization. Our formalism directly allows to consider superconducting weak links harboring more than two ABSs as well as spin-orbit coupling effects [18, 42]. Future work should clarify the role of Coulomb interactions, e.g., by modeling the weak link as a quantum dot [43–45].

We wish to thank J. Cerillo, M. Goffman, B. van Heck and J. J. Wesdorp for discussions. We acknowledge funding by FET-Open contract AndQC, the Deutsche Forschungsgemeinschaft (DFG, German Research Foundation) Grant No. 277101999 - TRR 183 (project C01), Grant No. EG 96/13-1, and under Germany’s Excellence Strategy - Cluster of Excellence Matter and Light for Quantum Computing (ML4Q) EXC 2004/1 - 390534769, and by the Spanish AEI through Grant No. PID2020-117671GB-I00 and through the “María de Maeztu” Programme for Units of Excellence in R&D (CEX2018-000805-M).

- 
- [1] Z.-L. Xiang, S. Ashhab, J. Q. You, and F. Nori, *Rev. Mod. Phys.* **85**, 623 (2013).
- [2] G. Wendin, *Reports on Progress in Physics* **80**, 106001 (2017).
- [3] M. Kjaergaard, M. E. Schwartz, J. Braumüller, P. Krantz, J. I.-J. Wang, S. Gustavsson, and W. D. Oliver, *Annual Review of Condensed Matter Physics* **11**, 369 (2020).
- [4] A. Blais, A. L. Grimsmo, S. M. Girvin, and A. Wallraff, *Rev. Mod. Phys.* **93**, 025005 (2021).
- [5] S. E. Rasmussen, K. S. Christensen, S. P. Pedersen, L. B. Kristensen, T. Bækkegaard, N. J. S. Loft, and N. T. Zinner, *PRX Quantum* **2**, 040204 (2021).
- [6] J. M. Martinis, M. Ansmann, and J. Aumentado, *Phys. Rev. Lett.* **103**, 097002 (2009).
- [7] A. D. Córcoles, J. M. Chow, J. M. Gambetta, C. Rigetti, J. R. Rozen, G. A. Keefe, M. Beth Rothwell, M. B. Ketchen, and M. Steffen, *Applied Physics Letters* **99**, 181906 (2011), <https://doi.org/10.1063/1.3658630>.
- [8] C. Wang, Y. Y. Gao, I. M. Pop, U. Vool, C. Axline, T. Brecht, R. W. Heeres, L. Frunzio, M. H. Devoret, G. Catelani, L. I. Glazman, and R. J. Schoelkopf, *Nature Communications* **5**, 5836 (2014).
- [9] M. Marín-Suárez, J. T. Peltonen, and J. P. Pekola, *Nano Letters* **20**, 5065 (2020), <https://doi.org/10.1021/acs.nanolett.0c01264>.
- [10] M. Zgirski, L. Bretheau, Q. Le Masne, H. Pothier, D. Esteve, and C. Urbina, *Phys. Rev. Lett.* **106**, 257003 (2011).
- [11] L. Bretheau, Ç. Ö. Girit, C. Urbina, D. Esteve, and H. Pothier, *Phys. Rev. X* **3**, 041034 (2013).
- [12] C. Janvier, L. Tosi, L. Bretheau, Ç. Ö. Girit, M. Stern, P. Bertet, P. Joyez, D. Vion, D. Esteve, M. F. Goffman, H. Pothier, and C. Urbina, *Science* **349**, 1199 (2015).
- [13] T. W. Larsen, K. D. Petersson, F. Kuemmeth, T. S. Jespersen, P. Krogstrup, J. Nygård, and C. M. Marcus, *Phys. Rev. Lett.* **115**, 127001 (2015).
- [14] G. de Lange, B. van Heck, A. Bruno, D. J. van Woerkom, A. Geresdi, S. R. Plissard, E. P. A. M. Bakkers, A. R. Akhmerov, and L. DiCarlo, *Phys. Rev. Lett.* **115**, 127002 (2015).
- [15] A. P. Higginbotham, S. Albrecht, G. Kiršanskas, W. Chang, F. Kuemmeth, P. Krogstrup, T. Jespersen, J. Nygård, K. Flensberg, and C. Marcus, *Nat. Phys.* **11**, 107 (2015).
- [16] D. J. van Woerkom, A. Proutski, B. van Heck, D. Bouman, J. I. Väyrynen, L. I. Glazman, P. Krogstrup, J. Nygård, L. P. Kouwenhoven, and A. Geresdi, *Nature Phys.* **13**, 876 (2017).
- [17] M. Hays, G. de Lange, K. Serniak, D. J. van Woerkom, D. Bouman, P. Krogstrup, J. Nygård, A. Geresdi, and M. H. Devoret, *Phys. Rev. Lett.* **121**, 047001 (2018).
- [18] L. Tosi, C. Metzger, M. F. Goffman, C. Urbina, H. Pothier, S. Park, A. L. Yeyati, J. Nygård, and P. Krogstrup, *Phys. Rev. X* **9**, 011010 (2019).
- [19] M. Hays, V. Fatemi, K. Serniak, D. Bouman, S. Diamond, G. de Lange, P. Krogstrup, J. Nygård, A. Geresdi, and M. H. Devoret, *Nature Phys.* **16**, 1103 (2020).
- [20] A. M. Whiticar, A. Fornieri, A. Banerjee, A. C. C. Drachmann, S. Gronin, G. C. Gardner, T. Lindemann, M. J. Manfra, and C. M. Marcus, *Phys. Rev. B* **103**, 245308 (2021).
- [21] M. Hays, V. Fatemi, D. Bouman, J. Cerrillo, S. Diamond, K. Serniak, T. Connolly, P. Krogstrup, J. Nygård, A. L. Yeyati, A. Geresdi, and M. H. Devoret, *Science* **373**, 430 (2021).
- [22] V. Fatemi, P. D. Kurilovich, M. Hays, D. Bouman, T. Connolly, S. Diamond, N. E. Frattini, V. D. Kurilovich, P. Krogstrup, J. Nygård, A. Geresdi, L. I. Glazman, and M. H. Devoret, *Phys. Rev. Lett.* **129**, 227701 (2022).
- [23] F. J. Matute-Cañadas, C. Metzger, S. Park, L. Tosi, P. Krogstrup, J. Nygård, M. F. Goffman, C. Urbina, H. Pothier, and A. L. Yeyati, *Phys. Rev. Lett.* **128**, 197702 (2022).
- [24] J. J. Wesdorp, L. Grünhaupt, A. Vaartjes, M. Pita-Vidal, A. Bargerbos, L. J. Splitthoff, P. Krogstrup, B. van Heck, and G. de Lange, *arXiv:2112.01936* (2021).
- [25] C. W. J. Beenakker and H. van Houten, *Phys. Rev. Lett.* **66**, 3056 (1991).
- [26] A. Furusaki and M. Tsukada, *Phys. Rev. B* **43**, 10164 (1991).
- [27] P. F. Bagwell, *Phys. Rev. B* **46**, 12573 (1992).
- [28] Y. V. Nazarov and Y. M. Blanter, *Quantum transport: Introduction to Nanoscience* (Cambridge University

- Press, Cambridge, 2009).
- [29] M. A. Despósito and A. Levy Yeyati, Phys. Rev. B **64**, 140511 (2001).
- [30] A. Zazunov, V. S. Shumeiko, E. N. Bratus', J. Lantz, and G. Wendin, Phys. Rev. Lett. **90**, 087003 (2003).
- [31] N. M. Chtchelkatchev and Y. V. Nazarov, Phys. Rev. Lett. **90**, 226806 (2003).
- [32] A. Zazunov, V. S. Shumeiko, G. Wendin, and E. N. Bratus', Phys. Rev. B **71**, 214505 (2005).
- [33] C. Padurariu and Y. V. Nazarov, Phys. Rev. B **81**, 144519 (2010).
- [34] F. Kos, S. E. Nigg, and L. I. Glazman, Phys. Rev. B **87**, 174521 (2013).
- [35] A. Zazunov, A. Brunetti, A. L. Yeyati, and R. Egger, Phys. Rev. B **90**, 104508 (2014).
- [36] D. G. Olivares, A. L. Yeyati, L. Bretheau, Ç. Ö. Girit, H. Pothier, and C. Urbina, Phys. Rev. B **89**, 104504 (2014).
- [37] R.-P. Riwar, M. Houzet, J. S. Meyer, and Y. V. Nazarov, Phys. Rev. B **91**, 104522 (2015).
- [38] S. Park, C. Metzger, L. Tosi, M. F. Goffman, C. Urbina, H. Pothier, and A. L. Yeyati, Phys. Rev. Lett. **125**, 077701 (2020).
- [39] See the online Supplementary Material (SM) which contains details of the derivation of our results and additional predictions of our theory.
- [40] U. Weiss, *Quantum Dissipative Systems*, 4th Edition (World Scientific, Singapore, 2012).
- [41] H.-P. Breuer and F. Petruccione, *The theory of open quantum systems*, (Oxford University Press, 2007).
- [42] S. Park and A. L. Yeyati, Phys. Rev. B **96**, 125416 (2017).
- [43] A. Martín-Rodero and A. L. Yeyati, Advances in Physics **60**, 899 (2011).
- [44] P. D. Kurilovich, V. D. Kurilovich, V. Fatemi, M. H. Devoret, and L. I. Glazman, Phys. Rev. B **104**, 174517 (2021).
- [45] C. Hermansen, A. L. Yeyati, and J. Paaske, Phys. Rev. B **105**, 054503 (2022).

## SUPPLEMENTAL MATERIAL

### MODEL

We consider a single-channel superconducting weak link described by the Hamiltonian (M1) (hereafter ‘‘M’’ indicates labels in the main text) together with a transfer matrix  $\hat{T}$  connecting the envelope functions,  $\Psi(0^-, t) = \hat{T}\Psi(0^+, t)$ . Using the notation in the main text, we have

$$\hat{T} = \frac{1}{\sqrt{\mathcal{T}}} \begin{pmatrix} e^{-i\tau_z \eta \hat{\theta}_R} & 0 \\ 0 & e^{i\tau_z \eta \hat{\theta}_R} \end{pmatrix} \begin{pmatrix} 1 & r \\ r & 1 \end{pmatrix} \times \begin{pmatrix} e^{-i\tau_z (1-\eta) \hat{\theta}_R} & 0 \\ 0 & e^{i\tau_z (1-\eta) \hat{\theta}_R} \end{pmatrix}, \quad (7)$$

where the parameter  $\eta \in [0, 1]$  determines the position of a local elastic scatterer in the normal-conducting weak link. In what follows, we consider the symmetric case  $\eta = 1/2$ , where Eq. (7) reduces to Eq. (M2). However, it is straightforward to adapt our formalism for  $\eta \neq 1/2$ .

With the gauge choice  $\phi_j(t) = s_j \varphi(t)/2$ , where  $s_{j=L/R} = \pm$ , and writing  $\varphi(t) = \varphi_0 + \tilde{\varphi}(t)$ , we next expand  $H_{L/R}$  in Eq. (M1) to linear order in the small phase fluctuations  $\tilde{\varphi}(t)$  caused by the electromagnetic environment. Applying the Josephson relation, we can use the auxiliary relation

$$V_j \tau_z + \Delta \tau_x e^{i\tau_z \phi_j} = e^{-is_j \tau_z \varphi_0/4} \times \left( \frac{s_j \tilde{\varphi}}{4} \tau_z + \frac{s_j \tilde{\varphi} \Delta}{2} \tau_y + \Delta \tau_x \right) e^{is_j \tau_z \varphi_0/4} + \mathcal{O}(\tilde{\varphi}^2). \quad (8)$$

In the next step, we gauge away  $\tilde{\varphi}$  from the matching condition (where  $\alpha = \pm$ ),

$$\psi_\alpha(0^\pm, t) \rightarrow e^{\pm i\alpha \tau_z \chi(t)/2} \psi_\alpha(0^\pm, t), \quad \chi = \frac{L}{4v_F} \dot{\tilde{\varphi}}, \quad (9)$$

taking into account that  $e^{i\hat{\theta}_R(t)} \approx e^{i\hat{\theta}(t)} e^{i\chi(t)} \approx e^{i\chi(t)} e^{i\hat{\theta}(t)}$  and neglecting all derivatives  $\partial_t^n \tilde{\varphi}$  with  $n \geq 2$ . At this point, we can expand  $H_j$  also to lowest order in  $\tilde{\varphi}$ , and finally remove  $\varphi_0$  from  $H_{L/R}$  by a gauge transformation, which correspondingly modifies the transfer matrix.

After the above sequence of steps, we obtain  $H(t) = H_0 + H_c(t)$ , with the fermion Hamiltonian

$$H_0 = \sum_{\pm} \int_{x \neq 0} dx \psi_{\pm}^{\dagger}(x) (\mp i v_F \tau_z \partial_x + \Delta \tau_x) \psi_{\pm}(x). \quad (10)$$

This noninteracting problem is diagonalized by solving the corresponding Bogoliubov-de Gennes (BdG) equations (M3), where the eigenenergies  $\epsilon_\nu$  and the corresponding spinor eigenstates  $\Psi_\nu(x)$  are given in Sec. below. We note that although the matching condition (7) is nonlocal in time, after the above expansion, we obtain a standard

stationary matching condition, see Eq. (M3). Below we employ a second-quantized description where the field operator,  $\hat{\Psi}(x) = \sum_{\nu} \Psi_\nu(x) \gamma_\nu$ , is expressed in terms of fermion annihilation operators  $\gamma_\nu$ . The noninteracting Hamiltonian is  $H_0 = \sum_{\nu} \epsilon_\nu \hat{n}_\nu$  with  $\hat{n}_\nu = \gamma_\nu^{\dagger} \gamma_\nu$ .

We find from the above steps that the coupling between fermionic quasiparticles and the electromagnetic environment is described by

$$H_c(t) = \sum_{\pm} \int_{x \neq 0} dx \psi_{\pm}^{\dagger}(x) U_{\pm}(x, t) \psi_{\pm}(x), \quad (11)$$

$$U_{\pm}(x, t) = \text{sgn}(-x) \left( \frac{\dot{\tilde{\varphi}}}{4} (\tau_z \mp \ell \tau_y) + \frac{\tilde{\varphi}}{2} \Delta \tau_y \right),$$

where  $\ell = L/\xi_0$ . Using the Josephson current operator  $\mathcal{I} = \sum_{\nu, \nu'} \mathcal{I}_{\nu\nu'} \gamma_\nu^{\dagger} \gamma_{\nu'}$  with the matrix elements (M4), we arrive at

$$H_c(t) = \frac{\tilde{\varphi}(t)}{2} \mathcal{I}(t) + \partial_t(\dots), \quad (12)$$

where the time derivative term does not affect the dynamics and can be omitted.

### QUASIPARTICLE SOLUTIONS

We next specify the quasiparticle spinor wave functions,  $\Psi_\nu(x)$ , and the corresponding eigenenergies,  $\epsilon_\nu$ , which follow by solving the BdG problem (M3). Here,  $\Psi = (\psi_+, \psi_-)^T$  is a bispinor in Nambu and left-right mover space. Because of the matching condition at  $x = 0^\pm$ , we have the unconventional normalization condition

$$\int_{-\infty}^{\infty} dx |\Psi_\nu(x)|^2 = 1 - \zeta_\nu, \quad (13)$$

$$\zeta_\nu = \frac{L}{2} (|\Psi_\nu(0^-)|^2 + |\Psi_\nu(0^+)|^2),$$

with  $L = \ell \xi_0$ . For continuum states, we find  $\zeta_\nu \sim \mathcal{O}(L/L_{\text{sc}}) \rightarrow 0$ , with the length  $L_{\text{sc}} \rightarrow \infty$  of the superconducting leads. However, for ABS solutions,  $\zeta_\nu$  must be accounted for in the normalization. In particular,  $\zeta_\nu$  can depend on  $\varphi_0$ . For notational ease, we set  $v_F = \Delta = 1$  below.

### Andreev bound states

For  $|\varepsilon| < 1$ , we have subgap ABS solutions with  $\nu \equiv \lambda$ , which can be written as

$$\Psi_\lambda(x) = \Theta(-x) e^{\kappa x} \begin{pmatrix} a \psi_h \\ b \psi_e \end{pmatrix} + \Theta(x) e^{-\kappa x} \begin{pmatrix} c \psi_e \\ d \psi_h \end{pmatrix}, \quad (14)$$

where  $\Theta(x)$  is the Heaviside step function and  $\psi_{e/h}$  are electron/hole-type Nambu spinors for localized states satisfying

$$(\varepsilon \mp i\kappa\tau_z - \tau_x)\psi_{e/h} = 0. \quad (15)$$

With  $\gamma = \cos^{-1}\varepsilon \in (0, \pi)$ , one finds

$$\kappa = \sin\gamma = \sqrt{1 - \varepsilon^2}, \quad \psi_{e/h} = \frac{e^{\pm i\tau_z\gamma/2}}{\sqrt{2}} \begin{pmatrix} 1 \\ 1 \end{pmatrix}. \quad (16)$$

From Eq. (13), the scalar amplitudes  $(a, b, c, d)$  in Eq. (14) obey the normalization condition  $|a|^2 + |b|^2 + |c|^2 + |d|^2 = 2\kappa/(1 + \ell\kappa)$ . The matching equations (M3) then yield the relations

$$\begin{aligned} \sqrt{\mathcal{T}}a &= e^{i\tau_z\gamma_+}c + re^{i\tau_z\varphi_0/2}d, \\ \sqrt{\mathcal{T}}b &= re^{i\tau_z\varphi_0/2}c + e^{-i\tau_z\gamma_-}d, \end{aligned} \quad (17)$$

where  $\gamma_{\pm} = \gamma - \theta \pm \varphi_0/2$  and  $\theta = \ell\varepsilon$ . Hence  $c$  and  $d$  follow from

$$\begin{pmatrix} \sin\gamma_+ & r\sin(\varphi_0/2) \\ r\sin(\varphi_0/2) & -\sin\gamma_- \end{pmatrix} \begin{pmatrix} c \\ d \end{pmatrix} = 0. \quad (18)$$

As a consequence, the dispersion equation for the phase-dependent ABS levels,  $\varepsilon = \varepsilon_{\lambda}(\varphi_0)$ , takes the form

$$\cos^{-1}(\varepsilon) - \ell\varepsilon \pm \sin^{-1}\left(\sqrt{\mathcal{T}}\sin(\varphi_0/2)\right) = \pi m \quad (19)$$

with  $m \in \mathbb{Z}$ . For each solution  $\varepsilon_{\lambda}$  with  $m = m_{\lambda}$ , another root of Eq. (19) is given by  $-\varepsilon_{\lambda}$  with  $m = 1 - m_{\lambda}$ .

### Continuum states

We next turn to above-gap states with quantum numbers  $\nu \equiv p = (\varepsilon, s)$  and  $|\varepsilon| > 1$ . Scattering state solutions for continuum quasiparticles can be written as the sum of incoming and outgoing plane waves,  $\Psi_p(x) = \Psi_p^{(\text{in})}(x) + \Psi_p^{(\text{out})}(x)$ . There are four incoming states labeled by  $s \in \{1, 2, 3, 4\}$ , which describe electron- or hole-type states injected from the left or right side,

$$\begin{aligned} \Psi_p^{(\text{in})}(x) &= \Theta(-x)\frac{e^{ikx}}{\sqrt{L_{\text{sc}}}} \left[ \delta_{s,1} \begin{pmatrix} \tilde{\psi}_e \\ 0 \end{pmatrix} + \delta_{s,2} \begin{pmatrix} 0 \\ \tilde{\psi}_h \end{pmatrix} \right] \\ &+ \Theta(x)\frac{e^{-ikx}}{\sqrt{L_{\text{sc}}}} \left[ \delta_{s,3} \begin{pmatrix} \tilde{\psi}_h \\ 0 \end{pmatrix} + \delta_{s,4} \begin{pmatrix} 0 \\ \tilde{\psi}_e \end{pmatrix} \right], \end{aligned} \quad (20)$$

and the respective four outgoing states,

$$\Psi_p^{(\text{out})}(x) = \Theta(-x)\frac{e^{-ikx}}{\sqrt{L_{\text{sc}}}} \begin{pmatrix} a_p\tilde{\psi}_h \\ b_p\tilde{\psi}_e \end{pmatrix} + \Theta(x)\frac{e^{ikx}}{\sqrt{L_{\text{sc}}}} \begin{pmatrix} c_p\tilde{\psi}_e \\ d_p\tilde{\psi}_h \end{pmatrix}. \quad (21)$$

Here  $\tilde{\psi}_{e/h}$  are electron/hole-type Nambu spinors for continuum states satisfying Eq. (15) with  $i\kappa \rightarrow k$ . Introducing  $\tilde{\gamma} = \sinh^{-1}(\sqrt{\varepsilon^2 - 1}) \in [0, \infty)$  and  $\sigma_{\varepsilon} = \text{sgn}(\varepsilon)$ , we write

$$\varepsilon = \sigma_{\varepsilon} \cosh\tilde{\gamma}, \quad k = \sigma_{\varepsilon} \sinh\tilde{\gamma}, \quad \tilde{\psi}_{e/h} = \frac{e^{\pm\tau_z\tilde{\gamma}/2}}{\sqrt{2\cosh\tilde{\gamma}}} \begin{pmatrix} 1 \\ \sigma_{\varepsilon} \end{pmatrix}. \quad (22)$$

Using

$$\sqrt{1 - (\varepsilon + i0^+)^2} = \kappa(\varepsilon)\Theta(1 - |\varepsilon|) - ik(\varepsilon)\Theta(|\varepsilon| - 1), \quad (23)$$

we observe that the eigenstates (14) and (21) are related by analytic continuation in the complex-energy plane, and the scalar amplitudes  $(a_p, b_p, c_p, d_p)$  again follow from matching conditions. With  $\theta = \ell\varepsilon$ ,

$$\begin{aligned} \sqrt{\mathcal{T}} \begin{pmatrix} a_p\tilde{\psi}_h + \delta_{s,1}\tilde{\psi}_e \\ b_p\tilde{\psi}_e + \delta_{s,2}\tilde{\psi}_h \end{pmatrix} &= e^{i\tau_z\varphi_0/2} \begin{pmatrix} e^{-i\tau_z\theta} & r \\ r & e^{i\tau_z\theta} \end{pmatrix} \\ &\times \begin{pmatrix} c_p\tilde{\psi}_e + \delta_{s,3}\tilde{\psi}_h \\ d_p\tilde{\psi}_h + \delta_{s,4}\tilde{\psi}_e \end{pmatrix}, \end{aligned} \quad (24)$$

with the normalization  $|a_p|^2 + |b_p|^2 + |c_p|^2 + |d_p|^2 = 1$ .

### Current matrix elements

We next provide explicit expressions for the supercurrent matrix elements (M4). First, for two ABSs with energies  $\varepsilon_{\lambda}$  and  $\varepsilon_{\lambda'}$ , using  $\gamma_{\lambda} = \cos^{-1}\varepsilon_{\lambda}$  and similarly for  $\gamma_{\lambda'}$ , we employ the relations

$$\begin{aligned} \psi_{e/h}^{(\lambda)\dagger} \tau_z \psi_{e/h}^{(\lambda')} &= \mp i \sin\left(\frac{\gamma_{\lambda} - \gamma_{\lambda'}}{2}\right), \\ \psi_{e/h}^{(\lambda)\dagger} \tau_y \psi_{e/h}^{(\lambda')} &= \mp \sin\left(\frac{\gamma_{\lambda} + \gamma_{\lambda'}}{2}\right). \end{aligned} \quad (25)$$

The matrix elements for ABS-ABS transitions follow with  $\omega_{\lambda\lambda'} = \varepsilon_{\lambda} - \varepsilon_{\lambda'}$  in the form

$$\begin{aligned} \mathcal{I}_{\lambda\lambda'} &= \left[ \frac{\omega_{\lambda\lambda'}}{2} \sin\left(\frac{\gamma_{\lambda} - \gamma_{\lambda'}}{2}\right) + \sin\left(\frac{\gamma_{\lambda} + \gamma_{\lambda'}}{2}\right) \right] \frac{a_{\lambda}^* a_{\lambda'} - b_{\lambda}^* b_{\lambda'} + c_{\lambda}^* c_{\lambda'} - d_{\lambda}^* d_{\lambda'}}{\sin\gamma_{\lambda} + \sin\gamma_{\lambda'}} \\ &+ i\ell \frac{\omega_{\lambda\lambda'}}{2} \sin\left(\frac{\gamma_{\lambda} + \gamma_{\lambda'}}{2}\right) \frac{a_{\lambda}^* a_{\lambda'} + b_{\lambda}^* b_{\lambda'} + c_{\lambda}^* c_{\lambda'} + d_{\lambda}^* d_{\lambda'}}{\sin\gamma_{\lambda} + \sin\gamma_{\lambda'}}. \end{aligned} \quad (26)$$

We next observe that in the limit  $L_{\text{sc}} \rightarrow \infty$ , matrix elements between continuum states,  $\Psi_p$  and  $\Psi_{p'}$ , can only be

finite if  $\varepsilon_p = \varepsilon_{p'}$ . However, the relations  $\tilde{\psi}_e^\dagger \tau_y \tilde{\psi}_e = \tilde{\psi}_h^\dagger \tau_y \tilde{\psi}_h = 0$  imply that such matrix elements vanish as well. We conclude that phase fluctuations cannot induce transitions between continuum states,  $\mathcal{I}_{pp'} = 0$ .

Finally, we discuss the matrix element connecting an ABS with energy  $\varepsilon_\lambda$  to a continuum state with energy  $\varepsilon_p$ . As in Eq. (22), we write  $\varepsilon_p = \sigma_{\varepsilon_p} \cosh \tilde{\gamma}_p$  and  $k_p = \sigma_{\varepsilon_p} \sinh \tilde{\gamma}_p$ . The matrix elements follow by using the relations

$$\psi_{e/h}^{(\lambda)\dagger} \tau_z \tilde{\psi}_{e/h} = \frac{w(\pm z^*)}{\sqrt{\cosh \tilde{\gamma}_p}}, \quad \psi_{e/h}^{(\lambda)\dagger} \tau_z \tilde{\psi}_{h/e} = \frac{w(\mp z)}{\sqrt{\cosh \tilde{\gamma}_p}}, \quad \psi_{e/h}^{(\lambda)\dagger} \tau_y \tilde{\psi}_{e/h} = \frac{iw(\pm z)}{\sqrt{\cosh \tilde{\gamma}_p}}, \quad \psi_{e/h}^{(\lambda)\dagger} \tau_y \tilde{\psi}_{h/e} = \frac{iw(\mp z^*)}{\sqrt{\cosh \tilde{\gamma}_p}},$$

with

$$z = (\tilde{\gamma}_p + i\gamma_\lambda)/2, \quad \omega_{p\lambda} = \varepsilon_p - \varepsilon_\lambda, \quad w(z) = \Theta(-\varepsilon_p) \cosh z + \Theta(\varepsilon_p) \sinh z, \quad W(z) = w(z) + \frac{\omega_{p\lambda}}{2} w^*(z).$$

Note that  $W(z^*) = W^*(z)$  and  $W(-z) = -\sigma_{\varepsilon_p} W(z)$ . We then obtain

$$\begin{aligned} \mathcal{I}_{\lambda p} = & \frac{i}{\sqrt{L_{\text{sc}} \cosh \tilde{\gamma}_p}} \left[ \frac{(a_\lambda^* a_p - d_\lambda^* d_p) W(-z) + (b_\lambda^* b_p - c_\lambda^* c_p) W(z)}{\sin \gamma_\lambda - ik_p} + \frac{(a_\lambda^* \delta_{s,1} - d_\lambda^* \delta_{s,4}) W(z^*) + (b_\lambda^* \delta_{s,2} - c_\lambda^* \delta_{s,3}) W(-z^*)}{\sin \gamma_\lambda + ik_p} \right] \\ & + \frac{\ell \omega_{p\lambda}}{2\sqrt{L_{\text{sc}} \cosh \tilde{\gamma}_p}} \left[ \frac{(a_\lambda^* a_p + d_\lambda^* d_p) w(-z) - (b_\lambda^* b_p + c_\lambda^* c_p) w(z)}{\sin \gamma_\lambda - ik_p} + \frac{(a_\lambda^* \delta_{s,1} + d_\lambda^* \delta_{s,4}) w(z^*) - (b_\lambda^* \delta_{s,2} + c_\lambda^* \delta_{s,3}) w(-z^*)}{\sin \gamma_\lambda + ik_p} \right]. \end{aligned}$$

Finally, we note that summations over  $p = (\varepsilon, s)$  are performed for  $L_{\text{sc}} \rightarrow \infty$  by using  $\frac{1}{L_{\text{sc}}} \sum_{p=(\varepsilon, s)} \dots = \int d\varepsilon \nu(\varepsilon) \sum_{s=1}^4 \dots$ , where  $\nu(\varepsilon)$  is the BCS density of states (per unit length) in the leads,  $\nu(\varepsilon) = \frac{1}{2\pi} \frac{|\varepsilon|}{\sqrt{\varepsilon^2 - 1}} \Theta(|\varepsilon| - 1)$ .

## MASTER EQUATION

We now describe the equations governing the ABS population dynamics. We begin by sketching the derivation of the Lindblad equation for the density operator  $\rho(t)$  describing the fermionic sector. Starting from the Hamiltonian  $H = H_0 + H_c + H_{\text{bath}}$ , the density matrix of the complete (system-plus-bath) system in the interaction picture,  $\tilde{\rho}_{\text{tot}}(t)$ , obeys the Liouville-von Neumann equation,

$$\begin{aligned} \dot{\tilde{\rho}}_{\text{tot}}(t) &= -i[H_c(t), \tilde{\rho}_{\text{tot}}(t)], \quad (27) \\ H_c(t) &= \frac{\tilde{\varphi}(t)}{2} \sum_{\nu, \nu'} e^{i\omega_{\nu\nu'} t} \mathcal{I}_{\nu\nu'} \gamma_\nu^\dagger \gamma_{\nu'}, \end{aligned}$$

with  $\omega_{\nu\nu'} = \varepsilon_\nu - \varepsilon_{\nu'}$ . Integrating Eq. (27) and inserting the result back into Eq. (27), we obtain

$$\begin{aligned} \dot{\tilde{\rho}}_{\text{tot}} &= - \int_0^t d\tau (H_c(t) [H_c(t-\tau), \tilde{\rho}_{\text{tot}}(t-\tau)] + \text{h.c.}) \\ &\quad - i[H_c(t), \tilde{\rho}_{\text{tot}}(0)]. \quad (28) \end{aligned}$$

Following Refs. [40, 41], we assume that the bath always remains in thermal equilibrium,  $\tilde{\rho}_{\text{tot}}(t) \approx \tilde{\rho}(t) \otimes \rho_{\text{bath}}$ , that the system-bath coupling is small (Born approximation), and that the bath has a very short memory time (Markov approximation). The reduced density matrix  $\tilde{\rho}(t)$  for the fermionic sector is obtained

by tracing over the bath,  $\tilde{\rho}(t) = \text{Tr}_{\text{bath}} \tilde{\rho}_{\text{tot}}(t)$ , resulting in

$$\dot{\tilde{\rho}} = \int_0^\infty d\tau \mathfrak{D}(\tau) [\mathcal{I}(t-\tau) \tilde{\rho}(t), \mathcal{I}(t)] + \text{h.c.} \quad (29)$$

with the bath correlation function

$$\mathfrak{D}(\tau) = \text{Tr}_{\text{bath}} \left( \rho_{\text{bath}} \frac{\tilde{\varphi}(t)}{2} \frac{\tilde{\varphi}(0)}{2} \right) = \mathfrak{D}^*(-\tau). \quad (30)$$

Writing  $\mathfrak{D}(\tau) = \int_{-\infty}^\infty \frac{d\omega}{2\pi} e^{-i\omega\tau} \mathfrak{D}_\omega$  and introducing a bath spectral density  $J(\omega) = -J(-\omega)$ , we can express  $\mathfrak{D}_\omega$  as

$$\mathfrak{D}_\omega = 2\pi J(\omega) (n_B(\omega) + 1), \quad (31)$$

with  $n_B(\omega) = 1/(e^{\omega/T_{\text{env}}} - 1)$ . Collecting the above results and switching to the Heisenberg picture, we arrive at a standard Lindblad equation [40, 41]

$$\dot{\rho} = -i[H_0, \rho] + \sum_{\nu \neq \nu'} \Gamma_{\nu\nu'} \mathcal{L}(Q_{\nu\nu'}) \rho, \quad (32)$$

with  $\mathcal{L}(Q)\rho = Q\rho Q^\dagger - \frac{1}{2} \{Q^\dagger Q, \rho\}$ . For the quasiparticle transition  $\nu \rightarrow \nu'$ , the jump operator  $Q_{\nu\nu'} = \gamma_{\nu'}^\dagger \gamma_\nu$  comes with the transition rate

$$\Gamma_{\nu\nu'} = 2\pi |\mathcal{I}_{\nu\nu'}|^2 J(\omega_{\nu\nu'}) [n_B(\omega_{\nu\nu'}) + 1]. \quad (33)$$

The spectral density  $J(\omega)$  describing the setup shown in Fig. M1(a) has been specified in Eq. (M5). With the notation  $\bar{\nu}$  for labeling the opposite-energy partner obtained by particle-hole symmetry,  $\varepsilon_{\bar{\nu}} = -\varepsilon_\nu$ , the rates (33) satisfy the symmetry relation  $\Gamma_{\bar{\nu}\bar{\nu}} = \Gamma_{\nu\nu}$ . In addition, forward and backward rates are linked by detailed balance,

$$\Gamma_{\nu\nu'} = e^{\omega_{\nu\nu'}/T_{\text{env}}} \Gamma_{\nu'\nu}. \quad (34)$$

	$gg$	$\sigma g$	$eg$	$ge$	$ee$	$\sigma\sigma$	$\sigma\bar{\sigma}$	$g\sigma$	$e\sigma$	$\sigma e$
$gg$	$-\tilde{\Gamma}_{gg}$	$\Gamma_{-1}^{\text{in}}$	$\Gamma_{1,-1}$	$\Gamma_{2,-2}$	0	0	$\Gamma_{1,-2}$	$\Gamma_{-2}^{\text{in}}$	0	0
$\sigma g$	$2\Gamma_1^{\text{in}}$	$-\tilde{\Gamma}_{\sigma g}$	$2\Gamma_{-1}^{\text{in}}$	0	0	$\Gamma_{-2}^{\text{in}}$	$\Gamma_{-2}^{\text{in}}$	$\Gamma_{-1,-2}$	$\Gamma_{1,-2}$	$\Gamma_{2,-2}$
$eg$	$\Gamma_{-1,1}$	$\Gamma_1^{\text{in}}$	$-\tilde{\Gamma}_{eg}$	0	$\Gamma_{2,-2}$	0	$\Gamma_{-1,-2}$	0	$\Gamma_{-2}^{\text{in}}$	0
$ge$	$\Gamma_{-2,2}$	0	0	$-\tilde{\Gamma}_{ge}$	$\Gamma_{1,-1}$	0	$\Gamma_{1,2}$	$\Gamma_2^{\text{in}}$	0	$\Gamma_{-1}^{\text{in}}$
$ee$	0	0	$\Gamma_{-2,2}$	$\Gamma_{-1,1}$	$-\tilde{\Gamma}_{ee}$	0	$\Gamma_{-1,2}$	0	$\Gamma_2^{\text{in}}$	$\Gamma_1^{\text{in}}$
$\sigma\sigma$	0	$\Gamma_2^{\text{in}}$	0	0	0	$-\tilde{\Gamma}_{\sigma\sigma}$	0	$\Gamma_1^{\text{in}}$	$\Gamma_{-1}^{\text{in}}$	$\Gamma_{-2}^{\text{in}}$
$\sigma\bar{\sigma}$	$2\Gamma_{-1,2}$	$\Gamma_2^{\text{in}}$	$2\Gamma_{1,2}$	$2\Gamma_{-1,-2}$	$2\Gamma_{1,-2}$	0	$-\tilde{\Gamma}_{\sigma\bar{\sigma}}$	$\Gamma_1^{\text{in}}$	$\Gamma_{-1}^{\text{in}}$	$\Gamma_{-2}^{\text{in}}$
$g\sigma$	$2\Gamma_2^{\text{in}}$	$\Gamma_{12}$	0	$2\Gamma_{-2}^{\text{in}}$	0	$\Gamma_{-1}^{\text{in}}$	$\Gamma_{-1}^{\text{in}}$	$-\tilde{\Gamma}_{g\sigma}$	$\Gamma_{1,-1}$	$\Gamma_{1,-2}$
$e\sigma$	0	$\Gamma_{-1,2}$	$2\Gamma_2^{\text{in}}$	0	$2\Gamma_{-2}^{\text{in}}$	$\Gamma_1^{\text{in}}$	$\Gamma_1^{\text{in}}$	$\Gamma_{-1,1}$	$-\tilde{\Gamma}_{e\sigma}$	$\Gamma_{-1,-2}$
$\sigma e$	0	$\Gamma_{-2,2}$	0	$2\Gamma_1^{\text{in}}$	$2\Gamma_{-1}^{\text{in}}$	$\Gamma_2^{\text{in}}$	$\Gamma_2^{\text{in}}$	$\Gamma_{-1,2}$	$\Gamma_{1,2}$	$-\tilde{\Gamma}_{\sigma e}$

TABLE II. Reduced  $10 \times 10$  rate matrix  $\mathbf{M}$  appearing in Eq. (40), expressed in terms of the transition rates  $\Gamma_{\lambda\lambda'}$  with ABS indices  $\lambda, \lambda' \in \{\pm 1, \pm 2\}$ , see Eq. (33), and the rates  $\Gamma_{\lambda}^{\text{in/out}}$  in Eq. (38).

In general, the Lindblad equation also contains an additional Lamb shift,  $H_L$ , such that  $H_0 \rightarrow H_0 + H_L$  in Eq. (32). The Lamb shift describes a renormalization of the quasiparticle energy levels. With Eq. (31), we find

$$H_L = \sum_{\nu \neq \nu'} Y(\omega_{\nu'\nu}) |\mathcal{I}_{\nu\nu'}|^2 Q_{\nu\nu'}^\dagger Q_{\nu\nu'}, \quad (35)$$

$$Y(\omega) = \text{p.v.} \int_{-\infty}^{\infty} \frac{d\omega'}{2\pi} \frac{\mathcal{D}_{\omega'}}{\omega - \omega'},$$

where ‘p.v.’ indicates a principal value integration. We note that  $H_L$  commutes with  $H_0$ . In fact,  $H_L$  does not enter the matrix rate equations (40) discussed below at all, and we therefore ignore Lamb shift contributions in what follows.

Following Ref. [35], we further simplify Eq. (32) by neglecting entanglement between Andreev and continuum states, i.e.,  $\rho(t) \simeq \rho_A(t) \otimes \rho_c$  with the reduced density matrix  $\rho_A(t)$  for the Andreev sector. Using a distribution function  $n_{p=(\varepsilon,s)}$  for parametrizing the continuum states, we write

$$\rho_c = \prod_p (n_p |1_p\rangle\langle 1_p| + (1 - n_p) |0_p\rangle\langle 0_p|), \quad (36)$$

Focusing on the case  $N = 2$ , we finally project Eq. (37) into the many-body Andreev states  $|\alpha, \beta\rangle$  listed in Table I of the main text. The off-diagonal components of  $\rho_A$  decouple from the diagonal elements in Eq. (37), which allows us to focus on the time evolution of the occupation probabilities  $P_{\alpha,\beta}(t) = \langle \alpha, \beta | \rho_A(t) | \alpha, \beta \rangle$ . The 16-dimensional vector  $\mathbf{P}(t)$  containing these probabilities then obeys a matrix rate equation,

$$\dot{\mathbf{P}} = \mathbf{M}\mathbf{P}, \quad (40)$$

with  $|1_p\rangle = \gamma_p^\dagger |0_p\rangle$ . After tracing Eq. (32) over the continuum states, the Andreev sector is described by

$$\dot{\rho}_A = -i[H_0, \rho_A] + \sum_{\lambda \neq \lambda'} \Gamma_{\lambda\lambda'} \mathcal{L}(Q_{\lambda'\lambda}) \rho_A \quad (37)$$

$$- \sum_{\lambda} \Gamma_{\lambda}^{\text{out}} \left( \frac{1}{2} \{ \hat{n}_{\lambda}, \rho_A \} - \gamma_{\lambda} \rho_A \gamma_{\lambda}^\dagger \right)$$

$$- \sum_{\lambda} \Gamma_{\lambda}^{\text{in}} \left( \frac{1}{2} \{ 1 - \hat{n}_{\lambda}, \rho_A \} - \gamma_{\lambda}^\dagger \rho_A \gamma_{\lambda} \right),$$

with  $\hat{n}_{\lambda} = \gamma_{\lambda}^\dagger \gamma_{\lambda}$  and the rates

$$\Gamma_{\lambda}^{\text{in}} = \sum_p \Gamma_{p\lambda} n_p, \quad \Gamma_{\lambda}^{\text{out}} = \sum_p \Gamma_{\lambda p} (1 - n_p), \quad (38)$$

which describe transitions from the continuum into the Andreev sector and vice versa. Below we model the presence of excess quasiparticles by a quasi-equilibrium Fermi distribution,

$$n_{p=(\varepsilon,s)} = \frac{1}{e^{\varepsilon/T_{\text{qp}}} + 1}, \quad (39)$$

where the quasiparticle temperature  $T_{\text{qp}}$  may differ from (and typically will exceed) the temperature  $T_{\text{env}}$  characterizing the electromagnetic environment.

where the real symmetric  $16 \times 16$  matrix  $\mathbf{M}$  is expressed in terms of the rates (33) and (38).

In our calculations, we make use of ‘‘spin’’ degeneracies of the many-body Andreev levels which allow us to reduce the effective matrix dimension for  $\mathbf{M}$  down to ten. (However, the resulting matrix is not symmetric anymore.) For this purpose, for  $\alpha \in \{g, e\}$ , we write

$$\tilde{P}_{\alpha,\sigma} = P_{\alpha,+} + P_{\alpha,-}, \quad \tilde{P}_{\sigma,\alpha} = P_{+,\alpha} + P_{-,\alpha}, \quad (41)$$

$$\tilde{P}_{\sigma,-\sigma} = P_{+,-} + P_{-,+}, \quad \tilde{P}_{\sigma,\sigma} = P_{+,+} + P_{-,-}.$$

Defining the 10-component vector  $\mathbf{P}(t) = (P_{g,g}, \tilde{P}_{\sigma,g}, P_{e,g}, P_{g,e}, P_{e,e}, \tilde{P}_{\sigma,\sigma}, \tilde{P}_{\sigma,\bar{\sigma}}, \tilde{P}_{g,\sigma}, \tilde{P}_{e,\sigma}, \tilde{P}_{\sigma,e})^T$ , the reduced  $10 \times 10$  matrix  $\mathbf{M}$  contains the transition rates  $\Gamma_{|\alpha,\beta\rangle \rightarrow |\alpha',\beta'\rangle}$  listed in Table III. The diagonal elements are  $-\tilde{\Gamma}_{\alpha\beta}$ , where the respective outgoing rates are given by

$$\begin{aligned}\tilde{\Gamma}_{g,g} &= \Gamma_{-1,1} + \Gamma_{-2,2} + 2(\Gamma_{-1,2} + \Gamma_1^{\text{in}} + \Gamma_2^{\text{in}}), \\ \tilde{\Gamma}_{e,g} &= \Gamma_{1,-1} + \Gamma_{-2,2} + 2(\Gamma_{1,2} + \Gamma_{-1}^{\text{in}} + \Gamma_2^{\text{in}}), \\ \tilde{\Gamma}_{g,e} &= \Gamma_{-1,1} + \Gamma_{2,-2} + 2(\Gamma_{-1,-2} + \Gamma_1^{\text{in}} + \Gamma_{-2}^{\text{in}}), \\ \tilde{\Gamma}_{e,e} &= \Gamma_{1,-1} + \Gamma_{2,-2} + 2(\Gamma_{1,-2} + \Gamma_{-1}^{\text{in}} + \Gamma_{-2}^{\text{in}}), \\ \tilde{\Gamma}_{\sigma,\sigma} &= \sum_{\lambda=\pm 1, \pm 2} \Gamma_{\lambda}^{\text{in}}, \\ \tilde{\Gamma}_{\sigma,\bar{\sigma}} &= \Gamma_{1,-2} + \Gamma_{1,2} + \Gamma_{-1,-2} + \Gamma_{-1,2} + \sum_{\lambda=\pm 1, \pm 2} \Gamma_{\lambda}^{\text{in}}, \\ \tilde{\Gamma}_{g,\sigma} &= \Gamma_{-1,-2} + \Gamma_{-1,1} + \Gamma_{-1,2} + 2\Gamma_1^{\text{in}} + \Gamma_2^{\text{in}} + \Gamma_{-2}^{\text{in}}, \\ \tilde{\Gamma}_{\sigma,g} &= \Gamma_{1,2} + \Gamma_{-1,2} + \Gamma_{-2,2} + 2\Gamma_2^{\text{in}} + \Gamma_1^{\text{in}} + \Gamma_{-1}^{\text{in}}, \\ \tilde{\Gamma}_{e,\sigma} &= \Gamma_{1,-1} + \Gamma_{1,-2} + \Gamma_{1,2} + 2\Gamma_{-1}^{\text{in}} + \Gamma_2^{\text{in}} + \Gamma_{-2}^{\text{in}}, \\ \tilde{\Gamma}_{\sigma,e} &= \Gamma_{1,-2} + \Gamma_{2,-2} + \Gamma_{-1,-2} + 2\Gamma_{-2}^{\text{in}} + \Gamma_1^{\text{in}} + \Gamma_{-1}^{\text{in}}.\end{aligned}$$

The steady-state solution,  $\mathbf{P}(\infty)$ , follows from  $\mathbf{M}\mathbf{P}(\infty) = 0$  together with normalization,  $\sum_{\alpha,\beta} P_{\alpha,\beta} = 1$ . We note in passing that for large  $T_{\text{qp}}/T_{\text{env}}$ , see Fig. M2(a), the ratio  $\Gamma_{\lambda=1}^{\text{in}}/\Gamma_{\lambda=1}^{\text{out}} \sim e^{(\Delta - \varepsilon_1)/T_{\text{env}}} n_p(\Delta)$  can exceed unity, which turns out to be a necessary condition for population inversion of the steady-state occupations. Given the time-dependent solution of Eq. (40), the parity-resolved total occupation probabilities are

$$P_{\text{even}}(t) = \sum_{\alpha,\beta \in \{g,e\}} P_{\alpha,\beta} + \sum_{\sigma,\sigma' \in \pm} P_{\sigma,\sigma'} \quad (42)$$

and  $P_{\text{odd}}(t) = 1 - P_{\text{even}}(t)$ .

In the main text, we assume a simplified picture for the time evolution of the state populations after an initial driving pulse whose frequency  $\Omega_d$  matches a specific (even or odd) transition. To that end, we imagine that the lower state is emptied by the pulse such that the corresponding steady-state population is completely transferred to the initial excited-state population. This procedure preserves the overall steady-state populations,  $P_{\text{even}}(0) = P_{\text{even}}(\infty)$  and likewise for  $P_{\text{odd}}$ . When driving, e.g., the transition  $|\sigma, g\rangle \rightarrow |g, \sigma\rangle$  (keeping in mind that states with  $\sigma = \pm$  are degenerate), this implies the initial condition

$$\tilde{P}_{g,\sigma}(0) = \tilde{P}_{\sigma,g}(\infty) + \tilde{P}_{g,\sigma}(\infty), \quad \tilde{P}_{\sigma,g}(0) = 0. \quad (43)$$

On the other hand, if the mixed even transition is driven, we only need to exchange the populations of the  $|g, g\rangle$  and the  $|\sigma, \bar{\sigma}\rangle$  states,

$$\tilde{P}_{\sigma,\bar{\sigma}}(0) = P_{g,g}(\infty) + \tilde{P}_{\sigma,\bar{\sigma}}(\infty), \quad P_{g,g}(0) = 0. \quad (44)$$

The results shown in the main text have been obtained under this simplified approach, where the driving pulse is taken into account via initial conditions for the matrix master equation. In order to compare these results to a more realistic scenario where the microwave pulse acts over an extended time duration [24], we have also studied the ABS population dynamics under a continuous microwave drive, see Sec. below.

## ROBUSTNESS AGAINST PARAMETER CHANGES

In this section, we provide additional results in order to test the robustness of the dynamical polarization effect with respect to changes in various parameters. Fig. 4 shows the time evolution of  $P_{\text{even,odd}}(t)$  after a driving pulse inducing the  $|g, g\rangle \rightarrow |\sigma, \bar{\sigma}\rangle$  transition. Panel (a) studies the effect of changing the transmission probability  $\mathcal{T}$  of the weak link. We observe that the achievable dynamical polarization is rather insensitive to  $\mathcal{T}$ , provided that the condition  $\Omega > \Delta - \varepsilon_2(\varphi_0)$  is met. However, with increasing  $\mathcal{T}$ , the time span during which the polarization of the odd-parity sector persists becomes shorter. Panel (b) shows the evolution of  $P_{\text{even/odd}}(t)$  with increasing environmental temperature  $T_{\text{env}}$ , where the growing thermal imbalance between the steady-state populations with even and odd parity comes along with a gradual decrease of the dynamical polarization. In particular, for  $T_{\text{env}} > T_{\text{qp}}$ , the state  $|e, g\rangle$  has increasingly large population probability. Finally, in panel (c), we monitor  $P_{\text{even/odd}}(t)$  as the resonator frequency  $\Omega$  is varied, where we find a decrease in the overall polarization with increasing  $\Omega$ . One can rationalize this observation by noting that at fixed temperature  $T_{\text{env}}$ , the average photon number in the resonator will decrease if  $\Omega$  is increased. Since fewer resonator photons are available for promoting a trapped quasiparticle into the continuum, the dynamical polarization will be reduced. In principle, one could increase it again by simply raising  $T_{\text{env}}$ . However, as detailed above, one needs to satisfy  $T_{\text{qp}} \gtrsim T_{\text{env}}$  at the same time.

## SPURIOUS DEGENERACIES

The ABS dispersion relation (19) predicts certain degeneracies between even and odd sector transitions. For instance, the  $|g, g\rangle \leftrightarrow |\sigma, \bar{\sigma}\rangle$  transition in the even sector is degenerate with the  $|\sigma, g\rangle \leftrightarrow |e, \sigma\rangle$  transition in the odd sector. Similarly, the  $|\sigma, g\rangle \leftrightarrow |g, \sigma\rangle$  transition in the odd sector matches the  $|e, g\rangle \leftrightarrow |\sigma, \bar{\sigma}\rangle$  transition in the even sector. If the drive frequency  $\Omega_d$  of the microwave pulse corresponds to degenerate transitions, the initial conditions for the matrix master equation, see Eqs. (43) and (44), have to be adapted accordingly.

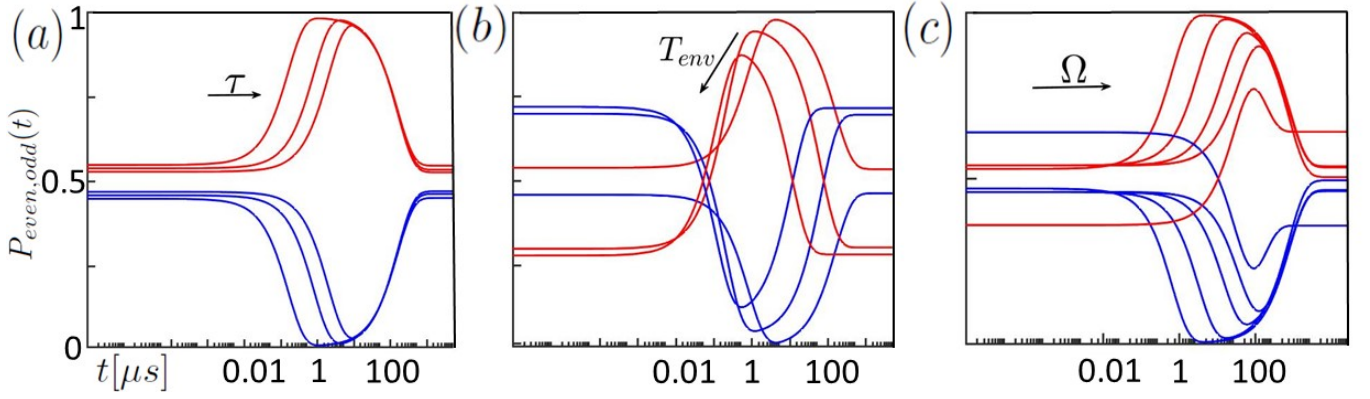


FIG. 4. Evolution of  $P_{\text{odd}}$  (red) and  $P_{\text{even}}$  (blue) vs time (in  $\mu\text{s}$  and on a logarithmic scale) after an initial microwave pulse inducing the mixed even transition,  $|g, g\rangle \rightarrow |\sigma, \bar{\sigma}\rangle$ . We use the parameters in Eq. (M6) together with  $\ell = 1.3$ ,  $\varphi_0 = \pi$ , and  $T_{\text{ap}} = 0.15\Delta$ . Panel (a) shows results for different transmission probabilities,  $\mathcal{T} = 0.45, 0.7, 0.9$ , with  $T_{\text{env}} = 0.07\Delta$ . Panel (b) illustrates the temperature dependence,  $T_{\text{env}}/\Delta = 0.07, 0.15, 0.22$ , with  $\mathcal{T} = 0.76$ . Panel (c) shows results for different resonator frequencies,  $\Omega/\Delta = 0.03, 0.2, 0.3, 0.7, 0.99$ , with  $T_{\text{env}} = 0.07\Delta$  and  $\mathcal{T} = 0.76$ . Arrows indicate increasing values for  $\mathcal{T}$ ,  $T_{\text{env}}$ , and  $\Omega$ , respectively.

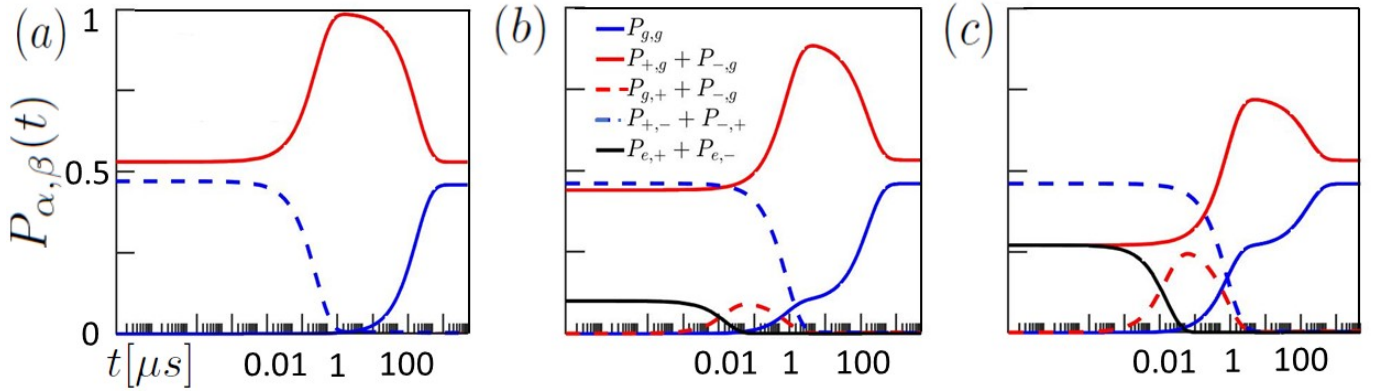


FIG. 5. Dynamical polarization after the initial microwave pulse for the same parameters as in Fig. M3(a). Panel (a) reproduces Fig. M3(a). Panels (b) and (c) illustrate the detrimental effect of simultaneously driving the transitions  $|g, g\rangle \leftrightarrow |\sigma, \bar{\sigma}\rangle$  and  $|\sigma, g\rangle \leftrightarrow |e, \sigma\rangle$ , which are degenerate in the absence of interactions. We use the initial state condition (44) with (b)  $\tilde{P}_{e,\sigma}(0) = 0.1$  and  $\tilde{P}_{\sigma,g}(0) = 0.44$ , or (c)  $\tilde{P}_{e,\sigma}(0) = \tilde{P}_{\sigma,g}(\infty)/2$  and  $\tilde{P}_{\sigma,g}(0) = \tilde{P}_{\sigma,g}(\infty)/2$ .

In practice, however, such degeneracies will be removed by spin-orbit coupling and Coulomb interaction effects. Indeed, according to Ref. [23], even a very weak Coulomb interaction, as expected for the open junction regime studied in Refs. [23, 24], will remove degeneracies in the even-sector transitions and change the relative position of the transition lines in the even and odd sectors. Taking as a reference the charging energy values quoted in Ref. [19], we estimate that the  $|g, g\rangle \rightarrow |\sigma, \bar{\sigma}\rangle$  and the  $|\sigma, g\rangle \rightarrow |e, \sigma\rangle$  transitions exhibit an energy splitting of the order of a few  $\mu\text{eV}$ , due to the Coulomb energy cost penalizing a double occupation of the lower ABS manifold in the  $|e, \sigma\rangle$  state. Although giving precise expressions for this splitting as a function of the model parameters is difficult, we safely estimate it to exceed the typical energy resolution in the present experiments. Leaving aside fine-tuned values of  $\varphi_0$  where accidental degeneracies occur,

we conclude that the simultaneous driving of degenerate transitions is not expected in actual experiments.

In the main text, we have implicitly assumed that degeneracies are lifted by such a mechanism. Nonetheless, Fig. 5 illustrates the detrimental effects that such simultaneous excitations would have on the dynamical polarization effect if a degeneracy is present. The extension of our theory to include spin-orbit coupling and/or Coulomb interaction effects is an important task for future research.

## CONTINUOUS MICROWAVE DRIVE

In the main text, we show results obtained by assuming that the microwave driving pulse can be described by initial conditions for the matrix master equation (40),

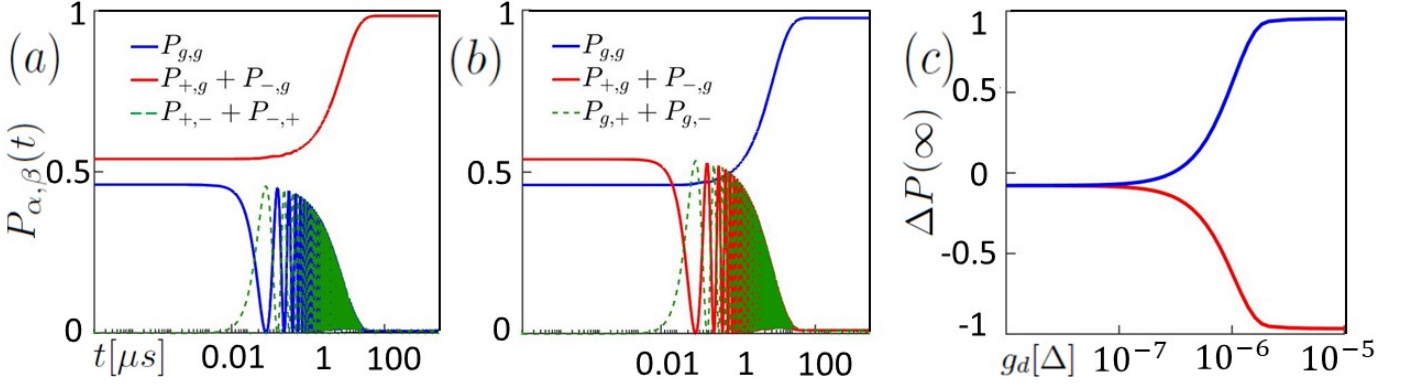


FIG. 6. Population dynamics,  $P_{\alpha,\beta}(t)$ , under a constant drive of amplitude  $g_d = 0.005\Delta$  for the parameters in Fig. M3(a). Panel (a) assumes a frequency  $\Omega_d$  in resonance with the transition  $|g, g\rangle \rightarrow |\sigma, \bar{\sigma}\rangle$ . Panel (b) assumes  $\Omega_d$  such that the transition  $|\sigma, g\rangle \rightarrow |g, \sigma\rangle$  is driven. Panel (c) shows the dependence of  $\Delta P(\infty) = P_{\text{even}}(\infty) - P_{\text{odd}}(\infty)$  on the drive amplitude  $g_d$ . The red [blue] line is for  $\Omega_d$  chosen as in panel (a) [(b)].

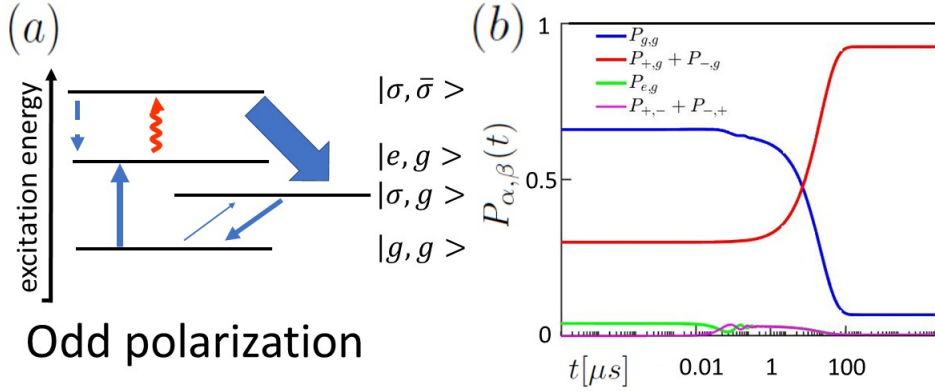


FIG. 7. Population dynamics under a constant drive of the  $|e, g\rangle \rightarrow |\sigma, \bar{\sigma}\rangle$  transition. Panel (a) illustrates the relevant transition rates between many-body Andreev states, cf. Fig. M1(c). The driving-induced rate is shown as red arrow. Panel (b) shows  $P_{\alpha,\beta}(t)$  for  $g_d = 0.005\Delta$ , using the parameters in Fig. M3(a) and  $T_{\text{env}} = 0.15\Delta$ .

see Eqs. (43) and (44). However, in actual experiments, see, e.g., Ref. [24], driving pulse effects could of course be more complex, and one may need to account for a finite pulse duration, the precise drive amplitude, or the detailed pulse shape. In the following, as a first step beyond the idealized initial condition approach used in the main text, we study the ABS population dynamics under a *continuous and resonant microwave drive* with drive amplitude  $g_d$ , where the drive frequency  $\Omega_d$  matches a transition between two specific many-body Andreev states  $|\alpha_1, \beta_1\rangle$  and  $|\alpha_2, \beta_2\rangle$ , with energies  $E_{\alpha_1, \beta_1} < E_{\alpha_2, \beta_2}$ , belonging to the same parity sector,

$$\Omega_d = E_{\alpha_2, \beta_2} - E_{\alpha_1, \beta_1}. \quad (45)$$

We here assume that the drive does not couple to other transitions. In particular, degeneracies should be lifted as described in Sec. . For  $\Omega_d > \Delta - \varepsilon_2$ , the driving field could in principle also cause transitions between the Andreev

sector and the quasiparticle continuum. However, unless the corresponding drive-induced transition rates exceed the fast (drive-independent) parity-changing rates shown in Fig. M1(c,d), such transitions will not have a qualitative impact on our results. In what follows, we consider weak drive amplitudes,  $g_d \ll \Delta$ , where this assumption is justified.

In order to model the continuous drive, we replace the effective Hamiltonian in the Lindblad equation (37) for the Andreev sector,  $H_0 \rightarrow H = H_0 + H_d$ . In the rotating wave approximation (RWA) and using the interaction picture, the drive Hamiltonian  $H_d$  for the frequency  $\Omega_d$  in Eq. (45) is given by

$$H_d = g_d |\alpha_2, \beta_2\rangle \langle \alpha_1, \beta_1| + \text{h.c.}, \quad (46)$$

where RWA is justified for  $g_d \ll \Omega_d$ . As explained above,  $H_d$  can then be truncated to include only transitions between the two many-body ABSs determining Eq. (45).

	$\alpha_1\beta_1$	$\alpha_2\beta_2$	$C_A$	$C_A^*$
$\alpha_1\beta_1$	0	0	$ig_d$	$-ig_d$
$\alpha_2\beta_2$	0	0	$-ig_d$	$ig_d$
$C_A$	$ig_d$	$-ig_d$	$-\tilde{\Gamma}_A$	0
$C_A^*$	$-ig_d$	$ig_d$	0	$-\tilde{\Gamma}_A$

TABLE III. Nonzero matrix elements of the matrix  $\mathbf{N}_d$  in Eq. (48).

After projecting Eq. (37) to the many-body ABS states  $|\alpha, \beta\rangle$ , we take into account only off-diagonal matrix elements of  $\rho_A$  (“coherences”) between the two states connected by the drive,  $C_A^{|\alpha_1, \beta_1\rangle \rightarrow |\alpha_2, \beta_2\rangle}(t)$ . For the three transitions studied below, they are defined as

$$\begin{aligned}
C_A^{|g, g\rangle \rightarrow |\sigma, \bar{\sigma}\rangle} &= \frac{1}{2} (\langle g, g | \rho_A | \sigma, \bar{\sigma} \rangle + \langle g, g | \rho_A | \bar{\sigma}, \sigma \rangle), \\
C_A^{|\sigma, g\rangle \rightarrow |g, \sigma\rangle} &= \frac{1}{2} (\langle +, g | \rho_A | g, + \rangle + \langle -, g | \rho_A | g, - \rangle), \\
C_A^{|e, g\rangle \rightarrow |\sigma, \bar{\sigma}\rangle} &= \frac{1}{2} (\langle e, g | \rho_A | \sigma, \bar{\sigma} \rangle + \langle e, g | \rho_A | \bar{\sigma}, \sigma \rangle). \quad (47)
\end{aligned}$$

Using the 12-dimensional vector  $\mathbf{W}(t) = (\mathbf{P}(t), C_A(t), C_A^*(t))^T$ , where the 10-dimensional vector  $\mathbf{P}(t)$  contains the occupation probabilities of the many-body ABSs as discussed in Sec. , the matrix master equation (40) then has to be replaced by the dynamical equation

$$\dot{\mathbf{W}}(t) = (\mathbf{M} + \mathbf{N}_d)\mathbf{W}(t), \quad (48)$$

where the matrix  $\mathbf{M}$  in Table II has been enlarged by zero columns and rows for the last two entries. The matrix  $\mathbf{N}_d$  has nonzero entries only for the four columns and rows referring to the ABS populations  $P_{\alpha_1, \beta_1}$  and  $P_{\alpha_2, \beta_2}$  or to coherences. The nonzero entries of  $\mathbf{N}_d$  are specified in Table III. For the transitions considered here, the coherence decay rates  $\tilde{\Gamma}_A$  are given by

$$\begin{aligned}
\tilde{\Gamma}_A^{|g, g\rangle \rightarrow |\sigma, \bar{\sigma}\rangle} &= \frac{1}{2} \left( \Gamma_{1,2} + \Gamma_{-1,2} + \Gamma_{1,-2} + \Gamma_{-1,2} + \Gamma_{2,1} \right. \\
&\quad \left. + \Gamma_{-1,1} + \Gamma_{-2,1} + \Gamma_{-2,2} + \Gamma_1^{\text{out}} + 2\Gamma_{-1}^{\text{out}} + \Gamma_{-2}^{\text{out}} \right. \\
&\quad \left. + 2\Gamma_2^{\text{in}} + \Gamma_{-2}^{\text{in}} + \Gamma_1^{\text{in}} \right), \quad (49) \\
\tilde{\Gamma}_A^{|\sigma, g\rangle \rightarrow |g, \sigma\rangle} &= \frac{1}{2} \left( \Gamma_{-2,1} + \Gamma_{1,2} + \Gamma_{-2,2} + \Gamma_{-1,1} + \Gamma_{2,1} \right. \\
&\quad \left. + \Gamma_1^{\text{out}} + 2\Gamma_{-1}^{\text{out}} + \Gamma_{-2}^{\text{out}} + 2\Gamma_2^{\text{in}} + \Gamma_{-2}^{\text{in}} + \Gamma_1^{\text{in}} \right), \\
\tilde{\Gamma}_A^{|e, g\rangle \rightarrow |\sigma, \bar{\sigma}\rangle} &= \frac{1}{2} \left( 3\Gamma_{1,2} + \Gamma_{-1,2} + \Gamma_{1,-2} + \Gamma_{2,1} + \Gamma_{1,-1} \right. \\
&\quad \left. + \Gamma_{-2,2} + 2\Gamma_1^{\text{out}} + \Gamma_{-1}^{\text{out}} + \Gamma_{-2}^{\text{out}} + 2\Gamma_2^{\text{in}} + \Gamma_{-2}^{\text{in}} + \Gamma_{-1}^{\text{in}} \right).
\end{aligned}$$

Numerical results for the ABS population dynamics under a continuous microwave drive of amplitude  $g_d = 0.005\Delta$  are shown in Fig. 6(a,b). In panel (a), the mixed even transition described above is resonantly driven, resulting in a polarization of the odd sector. We observe that the drive induces Rabi oscillations between the driven ABS states, which decay on a short time scale before the dynamical polarization behavior sets in. Since we have a continuous drive, the polarization of the odd sector then persists for long times. A similar picture is observed in panel (b), where  $\Omega_d$  matches the mixed odd transition  $|\sigma, g\rangle \rightarrow |g, \sigma\rangle$  and the even sector becomes polarized after an initial transient characterized by damped Rabi oscillations. For both cases, the dependence of the long-time polarization,  $\Delta P(\infty) = P_{\text{even}}(\infty) - P_{\text{odd}}(\infty)$ , on the drive amplitude is shown in Fig. 6(c). We observe that a rather weak drive amplitude,  $g_d \gtrsim 10^{-6}\Delta$ , is sufficient to induce the polarization effect, and the phenomenon then remains insensitive to the precise value of  $g_d$ . We therefore find basically the same behavior as obtained from the idealized initialization procedure. In particular, the respective peak polarization values are very close to the steady-state polarization values found under a continuous resonant drive with  $10^{-6}\Delta < g_d \ll \Omega_d$ . It is worth emphasizing that Fig. 6 also shows that our idealized initialization approach implicitly requires a sufficiently long pulse duration compared to the decay time of the Rabi oscillations. The latter is determined by the inverse of the rate  $\tilde{\Gamma}_A$  in Eq. (49).

Finally, we consider the effects of a continuous driving of transitions between higher-energy states. We have discussed above how to polarize the odd sector by driving the  $|g, g\rangle \rightarrow |\sigma, \bar{\sigma}\rangle$  transition. However, as illustrated in Fig. 7 for an elevated temperature  $T_{\text{env}}$ , if a small but finite steady-state population of the state  $|e, g\rangle$  is present, a polarization of the odd-parity sector can alternatively be generated by the smaller drive frequency,  $\Omega_d \approx \varepsilon_2 - \varepsilon_1$ . (For the case in Fig. M3(a), this also implies  $\Omega_d \approx \Delta - \varepsilon_1$ .) While in the absence of interactions, this transition is degenerate with the  $|\sigma, g\rangle \rightarrow |g, \sigma\rangle$  transition in the odd sector, even mild interactions can split both transitions. Such a mechanism may account for the behavior observed in Ref. [24] when driving with frequencies  $\sim 29$  GHz, just above the odd parity transition lines.